Characterization of Temporarily Captured Minimoon 2020 CD₃ by Keck Time-resolved Spectrophotometry

Bryce T. Bolin[1,2], Christoffer Fremling[1], Timothy R. Holt[3,4], Matthew J. Hankins[1], Tomás Ahumada[5], Shreya Anand[1], Varun Bhalerao[6], Kevin B. Burdge[1], Chris M. Copperwheat[7], Michael Coughlin[8], Kunal P. Deshmukh[9], Kishalay De[1], Mansi M. Kasliwal[1], Alessandro Morbidelli[10], Josiah N. Purdum[11], Robert Quimby[11,12], Dennis Bodewits[13], Chan-Kao Chang[14], Wing-Huen Ip[14], Chen-Yen Hsu[14], Russ R. Laher[2], Zhong-Yi Lin[14], Carey M. Lisse[15], Frank J. Masci[2], Chow-Choong Ngeow[14], Hanjie Tan[14], Chengxing Zhai[16], Rick Burruss[17], Richard Dekany[17], Alexandre Delacroix[17], Dmitry A. Duev[1], Matthew Graham[1], David Hale[17], Shrinivas R. Kulkarni[1], Thomas Kupfer[18], Ashish Mahabal[1,19], Przemyslaw J. Mróz[1], James D. Neill[1], Reed Riddle[17], Hector Rodriguez[17], Roger M. Smith[17], Maayane T. Soumagnac[20,21], Richard Walters[1], Lin Yan[1], and Jeffry Zolkower[17]

[1] Division of Physics, Mathematics and Astronomy, California Institute of Technology, Pasadena, CA 91125, USA; bbolin@caltech.edu
[2] IPAC, Mail Code 100-22, Caltech, 1200 E. California Blvd., Pasadena, CA 91125, USA
[3] University of Southern Queensland, Computational Engineering and Science Research Centre, Queensland, Australia
[4] Southwest Research Institute, Department of Space Studies, Boulder, CO 80302, USA
[5] Department of Astronomy, University of Maryland, College Park, MD 20742, USA
[6] Department of Physics, Indian Institute of Technology Bombay, Powai, Mumbai-400076, India
[7] Astrophysics Research Institute Liverpool John Moores University, 146 Brownlow Hill, Liverpool L3 5RF, UK
[8] School of Physics and Astronomy, University of Minnesota, Minneapolis, MN 55455, USA
[9] Department of Metallurgical Engineering and Materials Science, Indian Institute of Technology Bombay, Powai, Mumbai-400076, India
[10] Université Côte d'Azur, Observatoire de la Côte d'Azur, CNRS, Laboratoire Lagrange, Boulevard de l'Observatoire, CS 34229, F-06304 Nice cedex 4, France
[11] Department of Astronomy, San Diego State University, 5500 Campanile Dr., San Diego, CA 92182, USA
[12] Kavli Institute for the Physics and Mathematics of the Universe (WPI), The University of Tokyo Institutes for Advanced Study, The University of Tokyo, Kashiwa, Chiba 277-8583, Japan
[13] Physics Department, Leach Science Center, Auburn University, Auburn, AL 36832, USA
[14] Institute of Astronomy, National Central University, 32001, Taiwan
[15] Johns Hopkins University Applied Physics Laboratory, Laurel, MD 20723, USA
[16] Jet Propulsion Laboratory, California Institute of Technology, 4800 Oak Grove Dr., Pasadena, CA 91109, USA
[17] Caltech Optical Observatories, California Institute of Technology, Pasadena, CA 91125, USA
[18] Kavli Institute for Theoretical Physics, University of California, Santa Barbara, CA 93106, USA
[19] Center for Data Driven Discovery, California Institute of Technology, Pasadena, CA 91125, USA
[20] Lawrence Berkeley National Laboratory, 1 Cyclotron Rd., Berkeley, CA 94720, USA
[21] Department of Particle Physics and Astrophysics, Weizmann Institute of Science, Rehovot 76100, Israel

Abstract

We present time-resolved visible spectrophotometry of 2020 CD₃, the second known minimoon. The spectrophotometry was taken with the Keck I/Low Resolution Imaging Spectrometer between wavelengths 434 and 912 nm in the B, g, V, R, I, and RG850 filters as it was leaving the Earth–Moon system on 2020 March 23 UTC. The spectrum of 2020 CD₃ resembles V-type asteroids and some lunar rock samples with a 434–761 nm reddish slope of $\sim$18%/100 nm (g–r = 0.62 ± 0.08 and r–i = 0.21 ± 0.06) with an absorption band at $\sim$900 nm corresponding to i–z = −0.54 ± 0.10. Combining our measured H of 31.9 ± 0.1 with an albedo of 0.35 typical for V-type asteroids, we determine 2020 CD₃'s diameter to be $\sim$0.9 ± 0.1 m, making it the first minimoon and one of the smallest asteroids to be spectrally studied. We use our time-series photometry to detect significant periodic light-curve variations with a period of $\sim$573 s and amplitude of $\sim$1. In addition, we extend the observational arc of 2020 CD₃ to 37 days, to 2020 March 23 UTC. From the improved orbital solution for 2020 CD₃, we estimate the likely duration of its capture to be $\sim$2 yr and the nongravitational perturbation on its orbit due to radiation pressure with an area-to-mass ratio of (6.9 ± 2.4) × 10^{-4} m^2 kg^{-1} implying a density of 2.3 ± 0.8 g cm^{-3}, broadly compatible with other meter-scale asteroids and lunar rock. We searched for prediscovery detections of 2020 CD₃ in the Zwicky Transient Facility archive as far back as 2018 October but were unable to locate any positive detections.

Unified Astronomy Thesaurus concepts: Asteroids (72); Near-Earth objects (1092); Meteoroids (1040)

1. Introduction

Asteroid population models predict that out of $\sim$10⁹ asteroids larger than 1 m in the steady-state near-Earth object (NEO) population (Harris & D'Abramo 2015; Schunová-Lilly et al. 2017), a small fraction, $\sim$10⁻⁷, become temporarily captured by the Earth–Moon system's gravity every year (Granvik et al. 2012; Jedicke et al. 2018). These temporary natural satellites, or what we call "minimoons," have precapture orbital trajectories similar to the Earth that allow them to encounter the Earth at relatively low $\sim$1 km s⁻¹ speeds, assisting them in their capture. However, the captured status of the minimoon is temporary due to its interaction with the gravity of the Sun, the Earth–Moon system, and other massive solar system bodies, with the vast majority of minimoons only being gravitationally bound to the Earth–Moon system for $\sim$70–280 days (Fedorets et al. 2017). Since

they originate from the NEO population, the Earth–Moon system has a steady state of temporarily captured minimoons, with one to two being in orbit around the Earth at any given time with a diameter of ∼1 m. Out of ∼22,000 NEOs currently known,[22] only ∼five are in the 1 m range. Thus, due to their fRequency of capture and small size, minimoons provide the opportunity to study the smallest and most incomplete portion of the NEO population (Granvik et al. 2018). Also because of their low velocities relative to the Earth, minimoons provide excellent targets for human exploration missions (Elvis et al. 2011; Granvik et al. 2013; Chyba et al. 2014).

Asteroids on quasi-satellite orbits that are strongly affected by the gravitational influence of the Earth–Moon system but are not gravitationally captured have been observed before, such as 2013 LX28 and (469219) Kamoʻoalewa (Sidorenko et al. 2014; de la Fuente Marcos & de la Fuente Marcos 2016). However, the only previously known example of an asteroid being truly gravitationally captured by the Earth–Moon system was 2006 RH_{120}, discovered by the Catalina Sky Survey in 2006 while it was being captured by the Earth–Moon system's gravity. This first known minimoon remained in orbit around the Earth for ∼400 days (Kwiatkowski et al. 2008) and had a diameter of ∼3 m. Recently, the second known example of a temporarily captured asteroid was discovered on 2020 February 15 UTC with the Catalina Sky Survey's 1.5 m telescope (Pruyne et al. 2020).

At the time of discovery on 2020 February 15 UTC, 2020 CD_3 had a highly eccentric geocentrically bound orbit with a geocentric eccentricity, e_g, of 0.96; a geocentric semimajor axis, a_p, of ∼3 lunar distances (LDs) or ∼0.008 au, where 1 LD equals ∼0.00257 au; and a prograde geocentric inclination, i_g, of 49°. The majority of space debris or satellites of artificial origin are contained within 0.1 LD of the Earth, suggesting that the distant geocentric orbit of 2020 CD_3 is of natural origin (Tingay et al. 2013). It is possible for artificial objects, such as spacecraft boosters, to be on more distant geocentric orbits that may have trajectories similar to temporary natural orbits, such as J002E3, a possible Apollo program–era rocket booster (Jorgensen et al. 2003). The Minor Planet Center maintains a list of known spacecraft, as well as distant space debris;[23] however, none of these known spacecraft or distant space debris were associated with the trajectory of 2020 CD_3 at the time of its discovery (Pruyne et al. 2020).

While the initial orbit suggests a natural origin, determining the origin from within the solar system is less clear. As discussed above, NEO population models describe that the minimoon population originates from the Main Belt (Granvik et al. 2017); however, another possible natural origin of minimoons is lunar impacts due to the typical low, ∼1 km ejection speed of lunar debris (Gladman et al. 1995). The orbits of lunar debris dynamically decay after a few kyr, though it is possible that some lunar ejecta can be recaptured by the Earth–Moon system as minimoons due to their orbital similarity with the Earth, just as for minimoons of asteroidal origin (Granvik et al. 2012). However, it is currently unknown from the dynamical circumstances of lunar debris and temporarily captured asteroids what proportion of minimoons have an origin as the former to the latter.

In this paper, we build on the discovery of 2020 CD_3 with ground-based visible observations of it as an observational test to constrain whether it is of asteroidal or lunar debris origin. As we will discuss below, we will use the approach of Bolin et al. (2020) to combine estimation of its taxonomic classification from spectrophotometric observations at different visible wavelengths with its physical properties. In addition, we will use the astrometry from our observations of 2020 CD_3 to extend the orbital arc and refine the orbit of 2020 CD_3, enabling study of its dynamical evolution before, during, and after its capture by the Earth–Moon system. The refined orbit enabled by our observations will also serve as an independent constraint on its origin before being captured by the Earth–Moon system, as well as on its physical properties and origin by comparison with the NEO population model (Morbidelli et al. 2020) and estimation of nongravitational perturbations on its orbit (Mommert et al. 2014).

2. Observations

We used the 10 m Keck I telescope with the Low Resolution Imaging Spectrometer (LRIS; Oke et al. 1995; Rockosi et al. 2010) to observe 2020 CD_3 from 2020 March 23.545694 to March 23.583322 UTC in imaging mode (Program ID C236; PI: M. Fremling). Both the blue camera, consisting of a $2 \times 2K \times 4K$ Marconi CCD array, and the red camera, consisting of a science-grade Lawrence Berkeley National Laboratory $2K \times 4K$ CCD array, were used simultaneously. Both cameras have a spatial resolution of $0''135 \, \mathrm{pixel}^{-1}$ and were used in 2×2 binning mode, providing an effective resolution element size of $0''27$ providing a field of view of $6' \times 7'.8$. The 560 nm dichroic with ∼50% peak transmission was used in combination with the B ($\lambda_{\mathrm{eff}} = 435$ nm, FWHM of 91 nm), g ($\lambda_{\mathrm{eff}} = 474$ nm, FWHM of 98 nm), and V ($\lambda_{\mathrm{eff}} = 541$ nm, FWHM of 95 nm) filters for the blue camera. The R ($\lambda_{\mathrm{eff}} = 628$ nm, FWHM of 119 nm), I ($\lambda_{\mathrm{eff}} = 760$ nm, FWHM of 123 nm), and RG850 ($\lambda_{\mathrm{eff}} = 912$ nm, FWHM of 128 nm) filters, similar to the SDSS z filter ($\lambda_{\mathrm{eff}} = 905$ nm, FWHM of 137 nm; Fukugita et al. 1996), were used for the red camera in total with the blue camera, providing six total resolution elements between 435 and 912 nm.[24] Typical exposure times were ∼120 s and tracked nonsiderally at the ∼$3''$ minute^{-1} motion of 2020 CD_3. We rotated filters and used the two cameras simultaneously to limit the effect of rotational variations on photometric measurements. At the time of our observations, 2020 CD_3 was located near R.A., decl. = 14 20 00.3, +33 15 49.7 and had a heliocentric distance, r_h, of 1.0059 au; a geocentric distance, Δ, of 0.0128 au; and a phase angle, α, of 45°.4063. During our observations, the sky plane of motion of 2020 CD_3 was ∼$2''.5$ minute^{-1} and had an airmass of 1.03–1.08.

Images were taken of Solar-like calibrator stars identified using the Pan-STARRS catalog (Chambers et al. 2016; Flewelling et al. 2016) in nearby fields as 2020 CD_3. The seeing was ∼$0''.5$, and data from the Canada–France–Hawaii Telescope (CFHT) SkyProbe indicated that the night was photometrically stable with less than ∼0.01 mag variations over the course of our observations.[25] Bias and flat frames were obtained using the uniform flattening screen inside the Keck dome. The reduction of the imaging data was completed

---
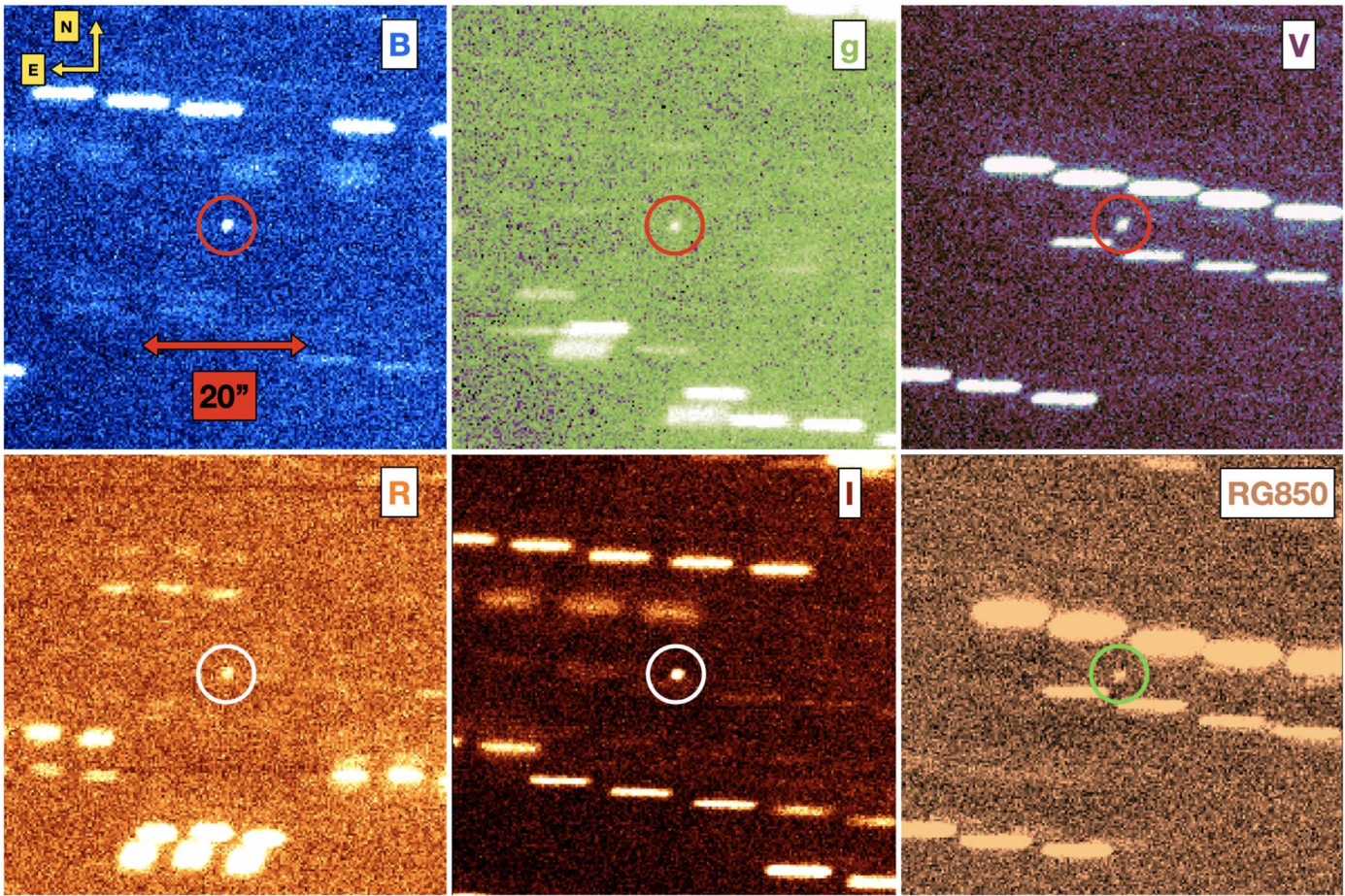
Figure 1. Top left panel: 600 s equivalent exposure time robust mean stack of 5 × 120 s *B*-filter images of 2020 CD_3. An arrow indicating the width of 20″ is shown for scale, and the cardinal directions are indicated. Top middle panel: 600 s equivalent exposure time robust mean stack of 4 × 120 s *g*-filter images of 2020 CD_3. Top right panel: 600 s equivalent exposure time robust mean stack of 5 × 120 s *V*-filter images of 2020 CD_3. Bottom left panel: 180 s equivalent exposure time mean stack of 3 × 60 s *R*-filter images of 2020 CD_3. Bottom middle panel: 960 s equivalent exposure time robust mean stack of 8 × 120 s *I*-filter images of 2020 CD_3. Bottom right panel: 600 s equivalent exposure time robust mean stack of 5 × 120 s RG850-filter images of 2020 CD_3.

using the LPipe reduction software (Perley 2019). 5 × 120 s *B* filter images, 5 × 120 s *g* filter images, 5 × 120 s *V* filter images, 3 × 30 s, 3 × 60 s *R* filter images, 8 × 120 s *I* filter images, and 5 × 120 s RG850 filter images were taken. Some images contained field stars near 2020 CD_3 that were discarded. The images were median-combined into separate composite stacks for all six filters, as shown in the image mosaic in Figure 1.

3. Results

3.1. Photometry and Spectral Classification

We measured the photometry of 2020 CD_3 and the solar analog stars using a 0″81 aperture subtracting the median contribution from the sky background within a 2″5–3″5 annulus. The *B*, *V*, *R*, and *I* Johnson–Cousins and *g* Sloan Digital Sky Survey (SDSS) filter photometry was calibrated using solar analog stars from the Pan-STARRS catalog (Chambers et al. 2016). The Pan-STARRS catalog magnitudes of the solar analog stars were transformed to Johnson–Cousins and SDSS magnitudes using the conversions from Tonry et al. (2012). We obtain magnitudes $B = 25.11 \pm 0.05$, $g = 24.48 \pm 0.05$, $V = 24.21 \pm 0.05$, $R = 23.74 \pm 0.06$, and $I = 23.31 \pm 0.02$. In addition, we determine an RG850 magnitude of 23.88 ± 0.09, calibrated by using the equivalent

SDSS *z*-filter magnitudes determined for our solar analog from the Pan-STARRS catalog. However, we caution that the RG850 and SDSS *z* filters are not exactly alike; therefore, our measured uncertainty is likely affected by small systematic differences between the RG850 and SDSS *z* filters and thus serves as a lower limit to its true RG850 magnitude.

The colors of 2020 CD_3 are $B–V = 0.90 \pm 0.07$, $V–g = -0.27 \pm 0.07$, $V–R = 0.46 \pm 0.08$, and $R–I = 0.44 \pm 0.06$. The equivalent colors in the SDSS bands are $g–r = 0.62 \pm 0.08$ and $r–i = 0.21 \pm 0.06$ using the filter transformations from Jordi et al. (2006). In addition, we determine an i–RG850 color of -0.54 ± 0.10. The *B–I* color of 2020 CD_3 is 1.80 ± 0.05, corresponding to a reflective spectral slope between 434 and 761 nm of $18\% \pm 3\%/100$ nm, indicating a surface significantly redder than the Sun ($B–I = 1.33$; Holmberg et al. 2006). In addition, the parameter $a^* = (0.89 (g–r)) + (0.45 (r–i)) - 0.57$, which is an indicator of reflective spectral slope (Ivezić et al. 2001), is equal to 0.08 ± 0.08 and plotted versus $i–z$(RG850) in Figure 2. Compared to other asteroids, the $a^* = 0.08 \pm 0.08$ and $i–z$(RG850) $= -0.54 \pm 0.10$ have broad overlap with other V-type asteroids, which have, on average, $a^* = 0.15 \pm 0.11$ and $i–z = -0.46 \pm 0.04$ (Jurić et al. 2002).

To compute the reflectivity spectrum of 2020 CD_3, we divide the flux per *B*, *g*, *V*, *R*, *I*, and RG850 filter obtained for 2020
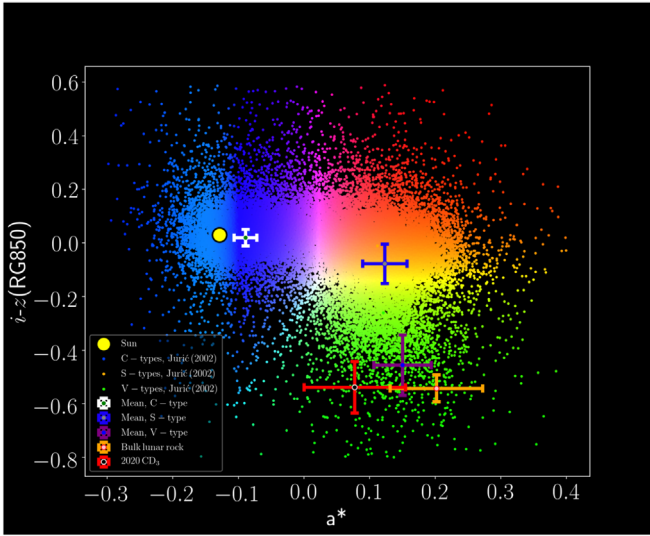
Figure 2. The a^* vs. i–z(RG850) colors of 2020 CD$_3$, plotted with the a^* vs. i–z colors of C-, S-, and V-type asteroids (Ivezić et al. 2001; Jurić et al. 2002), active comets (Solontoi et al. 2012), and Kuiper Belt objects (Ofek 2012). The colorization scheme of the data points as a function of a^* and i–z is adapted from Ivezić et al. (2002), where blue corresponds to C-type asteroids, red corresponds to S-type asteroids, and green corresponds to V-type asteroids. We note that in this case, the measured RG850 magnitude of 2020 CD$_3$ is plotted as a substitute for its z magnitude.

CD$_3$ by the flux of the solar analog flux in each corresponding filter. We then normalize the reflectivity spectrum to 550 nm and detrend the data using a fit of the spectrum with the function

$$r = 1 + a(\lambda - 550\,\text{nm}) \quad (1)$$

from Bus & Binzel (2002), where r is the normalized reflectivity as a function of λ and a is the spectral slope. The fit used to detrend the data from this function is made by fitting all B, g, V, R, I, and RG850 data between 435 and 912 nm. The resulting normalized reflectivity spectrum is plotted in Figure 3. The normalized reflectivity spectrum of 2020 CD$_3$ is most similar to the spectral range of V-type asteroids (Bus & Binzel 2002; DeMeo et al. 2009), with a red slope between 430 and a 760 nm deep absorption feature in the vicinity of the RG850 data point at $\sim$1000 nm compared to the reflectivity spectra of S- and C-type asteroids (DeMeo et al. 2009). We note the same similarity in a^* versus i–z(RG850) colors between 2020 CD$_3$ and V-type asteroids as seen in Figure 2 as with our normalized reflectivity spectrum. This absorption feature at $\sim$1000 nm, as seen for basaltic V-type asteroids found through the inner Main Belt, is due to the presence of large amounts of pyroxene minerals on the asteroid's surface (Moskovitz et al. 2008). In addition, we note the same similarity between the spectrum of 2020 CD$_3$ and bulk basaltic lunar rock consisting of pyroxene minerals (Isaacson et al. 2011).

3.2. Light-curve, Periodicity, and Axial Ratio Estimation

In addition to measuring the photometry of 2020 CD$_3$ in the per-filter B, g, V, R, I, and RG850 composite image stacks, we search for light-curve variations by measuring the photometry in our individual B-, g-, V-, and R-filter observations. The measured photometric values in the individual images are presented in
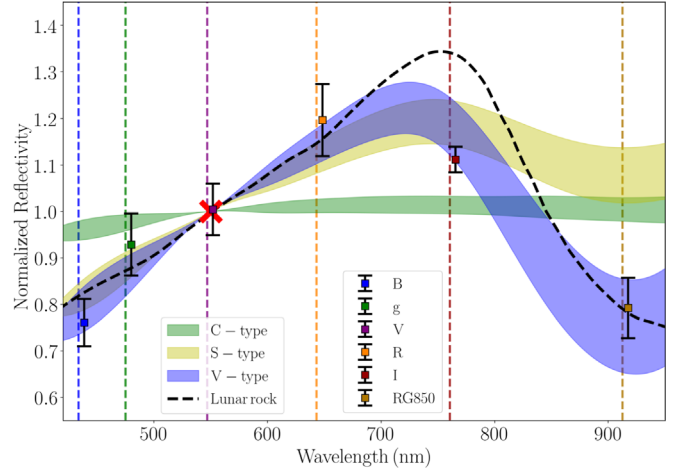
Figure 3. Reflectance photometric spectrum of 2020 CD$_3$ consisting of B, g, V, R, I, and RG850 observations of 2020 CD$_3$ on 2020 March 23 UTC. The λ_{eff} locations of the B, g, V, R, I, and RG850 filters have been plotted as vertical dashed lines. The data points for the normalized reflectivity of 2020 CD$_3$ have been offset slightly from their location in the wavelength direction. The error bars on the spectrum data points correspond to 1σ uncertainty. The spectrum has been normalized to unity at 550 nm, indicated by the red cross. The spectral range of S-, V-, and C-type asteroids from the Bus–DeMeo asteroid taxonomic catalog (DeMeo et al. 2009) is overplotted, with the V-type spectrum most closely resembling the spectra of 2020 CD$_3$. The average spectrum of coarse bulk lunar rock samples is plotted for reference (Isaacson et al. 2011).

Table 1
Summary of 2020 CD$_3$ Photometry Taken on 2020 March 23 UTC

Date[a] (MJD UTC)	Filter[b]	Exp[c] (s)	H[d]
58,931.5452386	R	60	31.39 ± 0.11
58,931.5456206	g	120	31.91 ± 0.17
58,931.5465002	R	60	32.33 ± 0.17
58,931.5477386	R	60	32.11 ± 0.16
58,931.5484447	g	120	32.13 ± 0.21
58,931.5489424	R	30	32.00 ± 0.13
58,931.5498336	R	30	31.50 ± 0.2
58,931.5520674	B	120	31.90 ± 0.12
58,931.5544632	B	120	32.35 ± 0.15
58,931.5599146	B	120	31.94 ± 0.12
58,931.5617317	B	120	31.89 ± 0.11
58,931.5643474	g	120	31.36 ± 0.11
58,931.566153	g	120	32.02 ± 0.19
58,931.5730511	V	120	31.80 ± 0.12
58,931.5749956	V	120	32.08 ± 0.16
58,931.5788613	V	120	31.90 ± 0.14

Notes.
[a] Observation date correct for light travel time.
[b] Keck I/LRIS filter.
[c] Exposure time.
[d] V-band equivalent H magnitude with 1σ uncertainties.

Table 1. We used the colors measured from our composite image stacks described in Section 3.1 and photospectrum to convert our B, g, and R measurements to their equivalent value in V. We use our V magnitudes and the equation

$$H = V - 5\log_{10}(r_h \Delta) \\ + 2.5\log_{10}[(1 - G)\Phi_1(\alpha) + G\,\Phi_2(\alpha)] \quad (2)$$
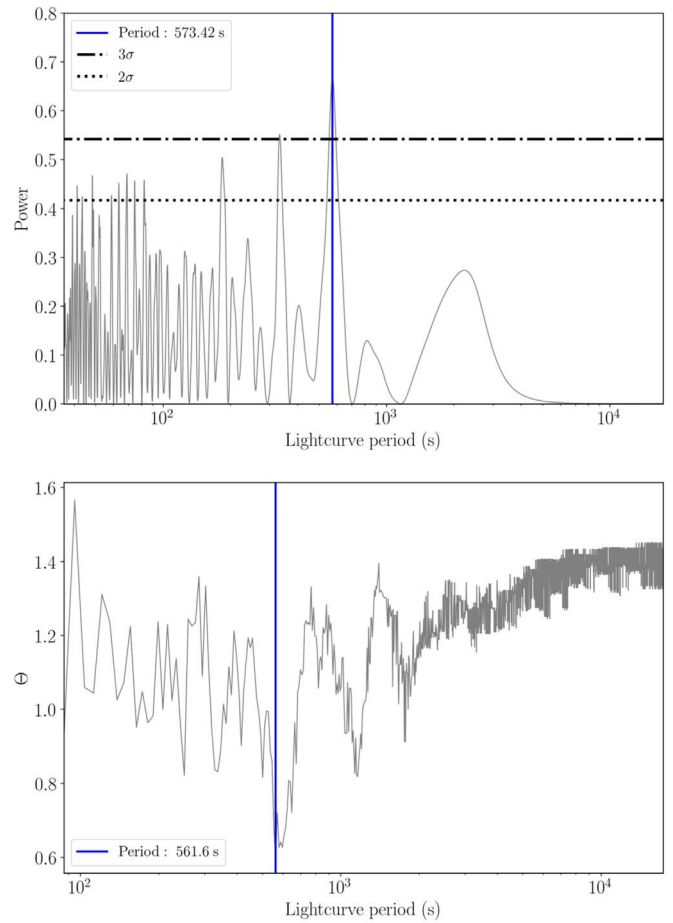
from Bowell et al. (1988), where r_h is the 1.0059 au heliocentric distance of 2020 CD$_3$ on 2020 March 23 UTC,
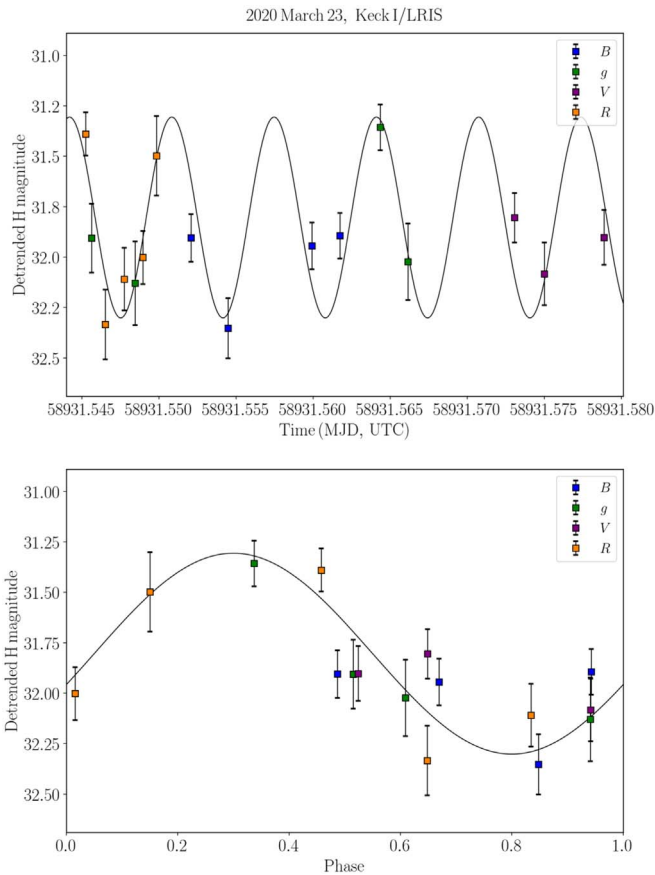
Figure 4. Top panel: detrended H-magnitude light curve from 2020 March 23 UTC Keck I/LRIS B, g, V, and R observations of 2020 CD_3 using a $0\rlap{.}''81$ radius aperture. The error bars on the data points are equal to their 1σ photometric uncertainties. The data have been detrended, and points affected by trailed background stars have been removed. The data points are color-coded by their filters. Bottom panel: phased 2020 March 23 UTC Keck I/LRIS observations corresponding to a single-peak light-curve period of 573.4 s.

Figure 5. Top panel: Lomb–Scargle periodogram of light-curve period vs. spectral power (Lomb 1976) for the Keck I/LRIS light-curve data from the 2020 March 23 UTC observations. A peak in the power is located at a double-peaked light-curve period of 573.4 s. Bottom panel: phase-dispersion minimization analysis of light-curve rotation period vs. Θ metric (Stellingwerf 1978). The Θ metric is minimized at a double-peaked rotation period of 561.6 s, consistent with the 573.4 s rotation period found with the Lomb–Scargle periodogram.

Δ is its geocentric distance of 0.0128 au, and α is its phase angle of $45\overset{\circ}{.}4063$. Here G is the phase coefficient, for which we use a value of 0.25, the average value of G for S- or Q-type asteroids (Vereš et al. 2015), and $\Phi_1(\alpha)$ and $\Phi_2(\alpha)$ are the basis functions normalized at $\alpha = 0°$ described in Bowell et al. (1988). We detrend the values of H inferred from Equation (2), dividing them by a linear fit that is plotted in the top panel of Figure 4 with a median value of $H = 31.9 \pm 0.1$. The errors on these H measurements may be underestimated, in part due to the unknown phase function of 2020 CD_3.

As seen in Figure 4, there is a brightness variability larger than the $\sim$0.01 photometric scatter measured from the CFHT SkyProbe and the typical $\sim$0.1 mag uncertainty of the data at a signal-to-noise ratio (S/N) of $\sim$10. Therefore, we will attempt to search for possible periodicities caused by time variability in 2020 CD_3's reflective cross section over its rotation (Barucci & Fulchignoni 1982). We apply the Lomb–Scargle periodogram (Lomb 1976) to the detrended H-magnitude data, which are displayed in the top panel of Figure 5. Removal of the linear trend over the $\sim$1 hr observing period will affect the determination of light-curve periods that are on $\sim$1 hr timescales but does not affect periodicities on $\sim$100 s time-scales. The highest peak in the light-curve period versus spectral power curve is located at $\sim$573.4 s with a formal

significance of $p \simeq 10^{-4}$. We apply bootstrap estimation (Press et al. 1986) of the uncertainties by removing $\sqrt{N}$ data points from the time-series light curve and repeating our periodogram estimation of the light-curve period 10,000 times, resulting in a central value of $\sim$574.5 s and a 1σ uncertainty estimate of $\sim$30.5 s. As an independent check of our results obtained with the Lomb–Scargle periodogram, we apply phase-dispersion minimization analysis to our data (Stellingwerf 1978) and obtain a result of $\sim$561.6 s, compatible with the light-curve period estimate obtained with the Lomb–Scargle periodogram as seen in the bottom panel of Figure 5. For comparison, the meter-scale asteroids 2006 RH_{120} and 2015 TC_{25} both had light-curve periods on the order of 60–120 s measured from photometry and radar observations. Furthermore, the ensemble of the available catalog of asteroid light-curve periods from the Asteroid Lightcurve Database (Warner et al. 2009) seems to indicate that asteroids smaller than 10 m can have rotation periods much shorter than 60 s (Bolin et al. 2014).

We can estimate a rough shape for 2020 CD_3 by assuming it possesses a triaxial prolate shape with dimensions a:b:c, where $b \geqslant a \geqslant c$, in rough approximation with the shapes of other asteroids inferred from light-curve inversion (Harris et al. 2009;

Durech et al. 2010). Assuming $a = c$, the ratio b/a is described by $b/a = 10^{0.4A}$, where A is the peak-to-trough light-curve amplitude (Binzel et al. 1989) resulting in a b/a of $\sim$2.5 for 2020 CD_3 with a light-curve amplitude of $\sim$1 mag. However, the combination of the significant phase angle of $\sim 45°$ that 2020 CD_3 was observed on 2020 March 23 UTC and the light-scattering properties of its presumably rough surface may have had the effect of amplifying its observed light-curve amplitude (Zappala et al. 1990). The relationship between the observed light-curve amplitude at a given phase angle α and the light-curve amplitude it would have if observed at $\alpha = 0°$ is given by

$$\Delta m_{\alpha=0°} = \frac{\Delta m(\alpha)}{1 + s\alpha} \quad (3)$$

from Zappala et al. (1990), where s is in units of mag deg^{-1}, for which we adopt the mean value of 0.012 mag deg^{-1} from the light-scattering experiment and observations of asteroids (Gutiérrez et al. 2006). Applying this correction to our observed light-curve amplitude of $\sim$1 mag, we calculate an equivalent $\alpha = 0°$ light-curve amplitude of $\sim$0.6 mag.

In addition to the relationship between phase angle and light-curve amplitude, the aspect angle of an asteroid when viewed from the Earth can also have an effect on its light-curve amplitude (e.g., Hanuš et al. 2018; Bolin & Lisse 2020). Because the pole orientation of 2020 CD_3 is unknown, it is not possible for us to constrain its aspect viewing angle. Therefore, we adopt the approach of Bolin et al. (2018c), which is to average over all possible aspect angles using the equation

$$\Delta m_{\mathrm{diff},\theta=90°} = 1.25 \log\left(\frac{b^2 \cos^2\theta + c^2 \sin^2\theta}{a^2 \cos^2\theta + c^2 \sin^2\theta}\right) \quad (4)$$

from Thirouin et al. (2016), which gives the light-curve amplitude of an asteroid when viewed equatorially, i.e., at an aspect angle of $\theta = 90°$, and where a, b, and c are the dimensions of 2020 CD_3. We will assume $1 \lesssim b/a \lesssim 2$, as observed in asteroid shape models inverted from light curves (Hanuš et al. 2013; Durech et al. 2015), and $a = c$ for a prolate triaxial ellipsoid. Integrating Equation (4) over all possible aspect angles results in $\Delta m_{\mathrm{diff}} \simeq 0.5$. Therefore, we calculate the b/a ratio of 2020 CD_3 using $b/a = 10^{0.4A}$, where $A = (\Delta m_{\alpha=0°} = 0.6$ from Equation (3) $+ \Delta m_{\mathrm{diff},\theta=90°} = 0.5$ from Equation (4)) $\simeq 1$, corresponding to $b/a \sim 2.5$ with the light-curve amplitude phase angle and aspect angle effects roughly canceling each other out.

3.3. Astrometry, Orbit Determination, and Archival Data Search

In addition to measuring the photometry from our observations, we use the positions of 2020 CD_3 measured in our 3×30 s R-filter images to refine the orbit of 2020 CD_3. We measured the astrometry of 2020 CD_3 with the Astrometrica software (Raab 2012) combined with reference stars from the Gaia Data Release 2 catalog (Gaia Collaboration et al. 2016, 2018). Table 2 contains our measured positions of 2020 CD_3 from our R-filter observations. We conservatively estimate an astrometric uncertainty of $1\rlap{.}''0$ in both the R.A. and decl. directions to take into account the $\sim$3 s timing uncertainty of the Keck I/LRIS instrument (Burdge et al. 2019), resulting in an increased $\sim 0\rlap{.}''2$ uncertainty in the along-track direction

measured for the position of 2020 CD_3 in addition to our nominal astrometric uncertainty of $\sim 0\rlap{.}''5$. Adding to our 2020 March 23 UTC observations, we combine our observations with the publicly available observations of 2020 CD_3 measured by other observatories from the Minor Planet Center observation database.[26] In total, we use 60 observations of 2020 CD_3 taken between 2020 February 18 UTC and 2020 March 23 UTC in addition to our own observations that are listed in Table 2. Although uncertainty estimates for other observatories' measurements of asteroids exist (Vereš & Chesley 2017), we adopt conservative estimates for the astrometric uncertainties of $\sim 1\rlap{.}''0$ in both R.A. and decl. for these other observatories' measured positions of 2020 CD_3. However, we adopt a positional uncertainty of $0\rlap{.}''4$ for the observations for 2020 CD_3 reported by T14, Maunakea, UH/Tholen NEO Follow-Up, made by the CFHT and $0\rlap{.}''8$ for observations made by J95, Great Shefford's 0.41 m telescope based on the historical astrometric performance made by these observatories described in the documentation for the orbit fitting software Find_Orb by Bill Gray.[27] We have submitted our astrometry of 2020 CD_3 on 2020 March 23 UTC to the Minor Planet Center, which has appeared in MPEC 2020-O103.[28]

Using Find_Orb, we fit an orbit to our list of observations using the eight planets and the Moon as perturbers. In addition to the six orbit parameters—semimajor axis, a; eccentricity, e; inclination, i; ascending node, Ω; argument of perihelion, ω; and mean anomaly, M—we include an additional parameter in our orbital fit, the area-to-mass ratio (AMR), as a measure of the effect of solar radiation pressure on the orbit of 2020 CD_3 (e.g., Micheli et al. 2012). The nominal orbital fit to our list of observations for the epoch of JD 2,458,931.5 (2020 March 23 UTC) in both heliocentric (a, e, i, Ω, ω, M) and geocentric (a_g, e_g, i_g, Ω_g, ω_g, M_g) orbital elements, the AMR and H magnitude are given in Table 3. It can be noted that the Earth-similar heliocentric elements of $a \sim 1$ au, $e \sim 0.02$, and low inclination are typical properties of the minimoon population (Granvik et al. 2012; Fedorets et al. 2017).

The mean observed-minus-computed residual from our least-squares orbital fit to the observations is $0\rlap{.}''40$, with the Keck I/LRIS observations having observed-minus-computed residuals of $\sim 0\rlap{.}''2$ using the seven orbital parameters (a, e, i, Ω, ω, M, AMR fit). By comparison, the six orbital parameter (a, e, i, Ω, ω, M) fit results in a slightly higher mean observed-minus-computed residual of $0\rlap{.}''43$. The complete list of observed-minus-computed residuals for each of the 60 observations used to compute the orbit is given in Table 2. The e_g of 0.95821 at the epoch of our orbital fit corresponding to the 2020 March 23 UTC data of our observations roughly indicates that 2020 CD_3's orbit was approaching an $e_g > 1$ hyperbolic state for leaving the Earth–Moon system, and the measured AMR of $(6.96 \pm 2.41) \times 10^{-4}$ m^2 kg^{-1} is comparable to other small asteroids with measured AMRs (e.g., Micheli et al. 2013; Mommert et al. 2014; Farnocchia et al. 2017). In addition, 2020 CD_3's i_g is retrograde, with a value of $146\rlap{.}°68615$ and a geocentric perihelion, q_g, of 0.00031 au, indicating that it is in the retrograde class of temporary natural satellites that come within the $\sim$0.01 au Hill radius of the Earth (Urrutxua & Bombardelli 2017; Jedicke et al. 2018).

---

[26] https://www.minorplanetcenter.net/tmp/2020_CD3.txt
[27] https://www.projectpluto.com/find_orb.htm
[28] https://minorplanetcenter.net/mpec/K20/K20OA3.html

Table 2
Summary of Astrometry from Observations Taken by Keck I/LRIS and Other Observatories between 2020 February 15 UTC and 2020 March 23 UTC

Date[a] (UTC)	R.A.[b]	Decl.[c]	$\sigma_{R.A.}$[d] (arcsec)	$\sigma_{decl.}$[e] (arcsec)	$X_{res.}$[f] (arcsec)	$Y_{res.}$[g] (arcsec)	Obs. Code[h]
2020 Feb 15.511140	13 03 33.110	+09 10 43.10	1.00	1.00	−0.33	−0.02	G96
2020 Feb 15.516240	13 03 34.520	+09 13 03.60	1.00	1.00	+0.07	+0.59	G96
2020 Feb 15.521330	13 03 35.960	+09 15 21.90	1.00	1.00	−0.50	+0.47	G96
2020 Feb 15.545470	13 03 44.540	+09 26 01.30	1.00	1.00	−0.17	−0.78	G96
2020 Feb 15.545640	13 03 44.640	+09 26 05.90	1.00	1.00	+0.27	−0.60	G96
2020 Feb 15.545820	13 03 44.700	+09 26 11.10	1.00	1.00	+0.06	−0.08	G96
2020 Feb 15.545990	13 03 44.770	+09 26 15.40	1.00	1.00	+0.05	−0.20	G96
2020 Feb 15.995517	13 18 35.410	+12 12 02.10	1.00	1.00	−0.36	+0.15	L01
2020 Feb 15.997407	13 18 36.130	+12 12 45.40	1.00	1.00	+0.05	+0.38	L01
2020 Feb 15.999831	13 18 36.990	+12 13 40.90	1.00	1.00	+0.02	+0.80	L01
2020 Feb 16.004013	13 18 38.390	+12 15 14.70	1.00	1.00	−0.30	−0.03	L01
2020 Feb 16.005639	13 18 38.940	+12 15 51.70	1.00	1.00	−0.02	+0.31	L01
2020 Feb 16.363950	13 25 20.450	+14 16 52.80	1.00	1.00	+0.26	+0.52	291
2020 Feb 16.366530	13 25 20.430	+14 17 41.60	1.00	1.00	+0.17	+0.61	291
2020 Feb 16.369160	13 25 20.380	+14 18 30.70	1.00	1.00	+0.09	+0.26	291
2020 Feb 16.437910	13 25 08.050	+14 38 18.00	1.00	1.00	+0.14	+0.05	I52
2020 Feb 16.439840	13 25 07.630	+14 38 49.70	1.00	1.00	+0.02	+0.18	I52
2020 Feb 16.441770	13 25 07.230	+14 39 20.80	1.00	1.00	+0.25	−0.15	I52
2020 Feb 16.443700	13 25 06.810	+14 39 52.00	1.00	1.00	+0.23	−0.25	I52
2020 Feb 17.040534	13 34 23.090	+16 43 52.20	1.00	1.00	+1.20	+0.32	L01
2020 Feb 17.046622	13 34 22.810	+16 45 14.60	1.00	1.00	−0.06	−0.01	L01
2020 Feb 17.051069	13 34 43.300	+16 40 45.90	0.80	0.80	−0.21	−0.02	J95
2020 Feb 17.054297	13 34 22.440	+16 46 58.00	1.00	1.00	+0.04	+0.44	L01
2020 Feb 17.070077	13 34 45.600	+16 45 07.30	0.80	0.80	+0.06	−0.33	J95
2020 Feb 17.084942	13 34 46.670	+16 48 26.90	0.80	0.80	−0.13	−0.01	J95
2020 Feb 17.100726	13 34 47.270	+16 51 52.70	0.80	0.80	+0.07	−0.36	J95
2020 Feb 17.508000	13 38 02.170	+18 18 19.10	1.00	1.00	+0.37	+0.61	G96
2020 Feb 17.510030	13 38 01.600	+18 18 36.30	1.00	1.00	+0.82	+0.12	G96
2020 Feb 17.512060	13 38 00.990	+18 18 54.50	1.00	1.00	+0.60	+0.76	G96
2020 Feb 17.514090	13 38 00.380	+18 19 11.50	1.00	1.00	+0.28	+0.32	G96
2020 Feb 17.980051	13 45 25.930	+19 19 39.42	1.00	1.00	−0.89	+0.35	Z84
2020 Feb 17.998253	13 45 29.233	+19 23 16.64	1.00	1.00	−0.80	−0.04	Z84
2020 Feb 18.016457	13 45 30.942	+19 26 49.53	1.00	1.00	−0.79	−0.11	Z84
2020 Feb 18.414650	13 47 52.480	+20 25 18.00	1.00	1.00	−0.09	+0.40	G96
2020 Feb 18.415230	13 47 52.300	+20 25 23.20	1.00	1.00	+0.17	+0.51	G96
2020 Feb 18.415810	13 47 52.140	+20 25 27.20	1.00	1.00	+0.54	−0.57	G96
2020 Feb 18.416390	13 47 51.930	+20 25 33.00	1.00	1.00	+0.21	+0.16	G96
2020 Feb 19.301670	13 55 16.820	+21 55 58.10	1.00	1.00	−0.51	+0.82	G96
2020 Feb 19.303920	13 55 16.910	+21 56 17.50	1.00	1.00	+0.23	−0.70	G96
2020 Feb 19.306180	13 55 16.960	+21 56 39.00	1.00	1.00	+0.71	−0.15	G96
2020 Feb 20.418810	14 00 29.620	+23 35 56.90	1.00	1.00	−0.02	+0.59	G96
2020 Feb 20.419560	14 00 29.390	+23 36 00.70	1.00	1.00	+0.44	−0.01	G96
2020 Feb 20.420320	14 00 29.140	+23 36 05.20	1.00	1.00	+0.69	+0.05	G96
2020 Feb 20.421070	14 00 28.880	+23 36 11.00	1.00	1.00	+0.76	+0.97	G96
2020 Feb 21.095901	14 03 49.976	+24 21 03.47	1.00	1.00	−0.39	−0.35	Z84
2020 Feb 21.120492	14 03 42.513	+24 23 16.74	1.00	1.00	−0.47	−0.68	Z84
2020 Feb 21.146268	14 03 33.897	+24 25 23.50	1.00	1.00	+0.03	−0.04	Z84
2020 Feb 21.172268	14 03 24.721	+24 27 15.50	1.00	1.00	+0.09	−0.23	Z84
2020 Feb 21.196581	14 03 16.142	+24 28 46.33	1.00	1.00	+0.54	−0.46	Z84
2020 Feb 27.642330	14 19 58.612	+29 10 39.85	0.40	0.40	+0.00	+0.01	T14
2020 Feb 27.643742	14 19 58.040	+29 10 40.82	0.40	0.40	−0.01	+0.01	T14
2020 Feb 27.645156	14 19 57.468	+29 10 41.76	0.40	0.40	−0.04	+0.02	T14
2020 Mar 01.477510	14 23 44.930	+30 15 25.40	1.00	1.00	+0.40	−0.33	G37
2020 Mar 01.479210	14 23 44.270	+30 15 27.40	1.00	1.00	−0.36	−0.14	G37
2020 Mar 01.480250	14 23 43.970	+30 15 28.30	1.00	1.00	+0.52	−0.32	G37
2020 Mar 22.483420	14 21 40.530	+33 16 25.12	0.40	0.40	−0.04	+0.00	T14
2020 Mar 22.487379	14 21 38.999	+33 16 27.56	0.40	0.40	+0.03	+0.01	T14
2020 Mar 23.544957	14 20 00.300	+33 15 49.70	1.00	1.00	+0.03	+0.01	568
2020 Mar 23.548839	14 19 58.780	+33 15 48.50	1.00	1.00	−0.10	−0.13	568
2020 Mar 23.549729	14 19 58.420	+33 15 47.90	1.00	1.00	+0.28	+0.13	568

Notes.
[a] UTC observation date at the midpoint of the exposure.
[b] Right ascension.
[c] Declination.
[d] Uncertainty in R.A.
[e] Uncertainty in decl.
[f] Observed-minus-computed residual in the X direction.
[g] Observed-minus-computed residual in the Y direction.
[h] Minor Planet Center Observatory Code.

Table 3
Orbital Elements of 2020 CD_3 Based on Observations Collected between 2020 February 15 UTC and 2020 March 23 UTC

Heliocentric Elements	
Epoch (JD)	2,458,931.5
Time of perihelion, T_p (JD)	$2,458,907.045 \pm (0.019)$
Semimajor axis, a (au)	$1.01713 \pm (6.49 \times 10^{-7})$
Eccentricity, e	$0.02858 \pm (6.58 \times 10^{-7})$
Perihelion, q (au)	$0.98806 \pm (6.51 \times 10^{-8})$
Aphelion, Q (au)	$1.04620 \pm (1.34 \times 10^{-6})$
Inclination, i (deg)	$0.55483 \pm (1.80 \times 10^{-5})$
Ascending node, Ω (deg)	$116.954 \pm (1.70 \times 10^{-3})$
Argument of perihelion, ω (deg)	$357.557 \pm (1.30 \times 10^{-3})$
Mean anomaly, M (deg)	$65.1632 \pm (4.44 \times 10^{-4})$
Geocentric Elements	
Epoch (JD)	2,458,931.5
Time of perihelion, $T_{p,g}$ (JD)	$2,458,893.615 \pm (7.47 \times 10^{-5})$
Semimajor axis, a_g (au)	$0.00752 \pm (3.72 \times 10^{-7})$
Eccentricity, e_g	$0.95821 \pm (9.88 \times 10^{-7})$
Perihelion, q_g (au)	$0.00031 \pm (2.05 \times 10^{-8})$
Aphelion, Q_g (au)	$0.01472 \pm (7.24 \times 10^{-7})$
Inclination, i_g (deg)	$146.68615 \pm (7.24 \times 10^{-7})$
Ascending node, Ω_g (deg)	$309.888 \pm (5.5 \times 10^{-4})$
Argument of perihelion, ω_g (deg)	$280.529 \pm (1.0 \times 10^{-3})$
Mean anomaly, M_g (deg)	$99.299 \pm (7.0 \times 10^{-3})$
AMR ($m^2 kg^{-1}$)	$6.96 \times 10^{-4} \pm (2.41 \times 10^{-4})$
Absolute magnitude, H	$31.9 \pm (0.1)$

Note. The orbital elements are shown for the Julian Date (JD) using the software Find_Orb by Bill Gray. The 1σ uncertainties are given in parentheses.

Our refined orbital solution of 2020 CD_3 from our 2020 March 23 UTC observations enabled the search for possible prediscovery detections of 2020 CD_3 in the Zwicky Transient Facility (ZTF) archive (Masci et al. 2019) for additional refinement of the orbit (e.g., similar as for prediscovery observations interstellar object 2I/Borisov by ZTF Bolin et al. 2020; Ye et al. 2020). The ZTF survey, based on the Palomar Observatory's P48 Oschin Schmidt telescope, consists of a number of survey programs, some that are open to the public and some that are internal to the ZTF collaboration and Caltech, that are designed to cover the entire sky and detect transient sources, including solar system asteroids and comets (Graham et al. 2019). The ZTF survey camera consists of a 576 megapixel array with a pixel scale of $1{.}''01$ pixel^{-1} covering a $7{.}°4 \times 7{.}°4$ field of view (Dekany et al. 2016) and g-, r-, and i-band filters with $r \sim 20.5$ to an S/N = 5 depth in a 30 s exposure generally used in the survey (Bellm et al. 2019). The ZTF data system has the ability to detect both round, point-spread function–like detections (Masci et al. 2019) and fast-moving objects moving $>5''$ m^{-1}, resulting in the detections becoming significantly trailed (Duev et al. 2019; Ye et al. 2019b) in the survey's 30 s exposures. Therefore, because of its large field of view and ability to identify fast-moving objects, ZTF is the ideal system for ground-based detection of minimoons, objects that typically move $>10''$ minute^{-1} or more (Bolin et al. 2014; Fedorets et al. 2020).

Extrapolating the trajectory of 2020 CD_3 as far back as 2018 October, we located regions of the sky where it was covered by the ZTF survey in the g and r filters. We narrowed our search for prediscovery observations to times when 2020 CD_3 was brighter than $V \sim 20$, taking into account the ~ 0.2 mag mean color differences between the standard Johnson V filter and the ZTF r filter for asteroids (Vereš & Chesley 2017). Our search revealed the dates when 2020 CD_3 was brighter than $V \sim 20$ as 2019 January 17 UTC ($V \sim 19.1$), 2019 April 4 UTC ($V \sim 15.2$), 2019 November 15 UTC ($V \sim 19.5$) and 2020 February 13 UTC ($V \sim 17.0$). However, the only date overlapping with ZTF observations was 2019 November 15 UTC, on which a single g-band exposure was obtained; this was also during the full phase of the moon, greatly increasing the sky background in the image. In addition, 2020 CD_3 was moving nearly $\sim 40''$ minute^{-1}, resulting in significant trailing losses (Shao et al. 2014) and making its already difficult brightness of $V \sim 19.5$ impossible to detect. A possible method of detection for 2020 CD_3 is to use where its orbital trajectory overlaps with higher-cadence fields while it is moving with a slower rate of motion and synthetic tracking to shift and stack along its possible trajectories, increasing its detection's S/N to a detectable threshold, as has been demonstrated for ZTF data of the Main Belt and NEOs (Zhai et al. 2020); however, a full demonstration of synthetic tracking to locate 2020 CD_3 in ZTF data is beyond the scope of this work.
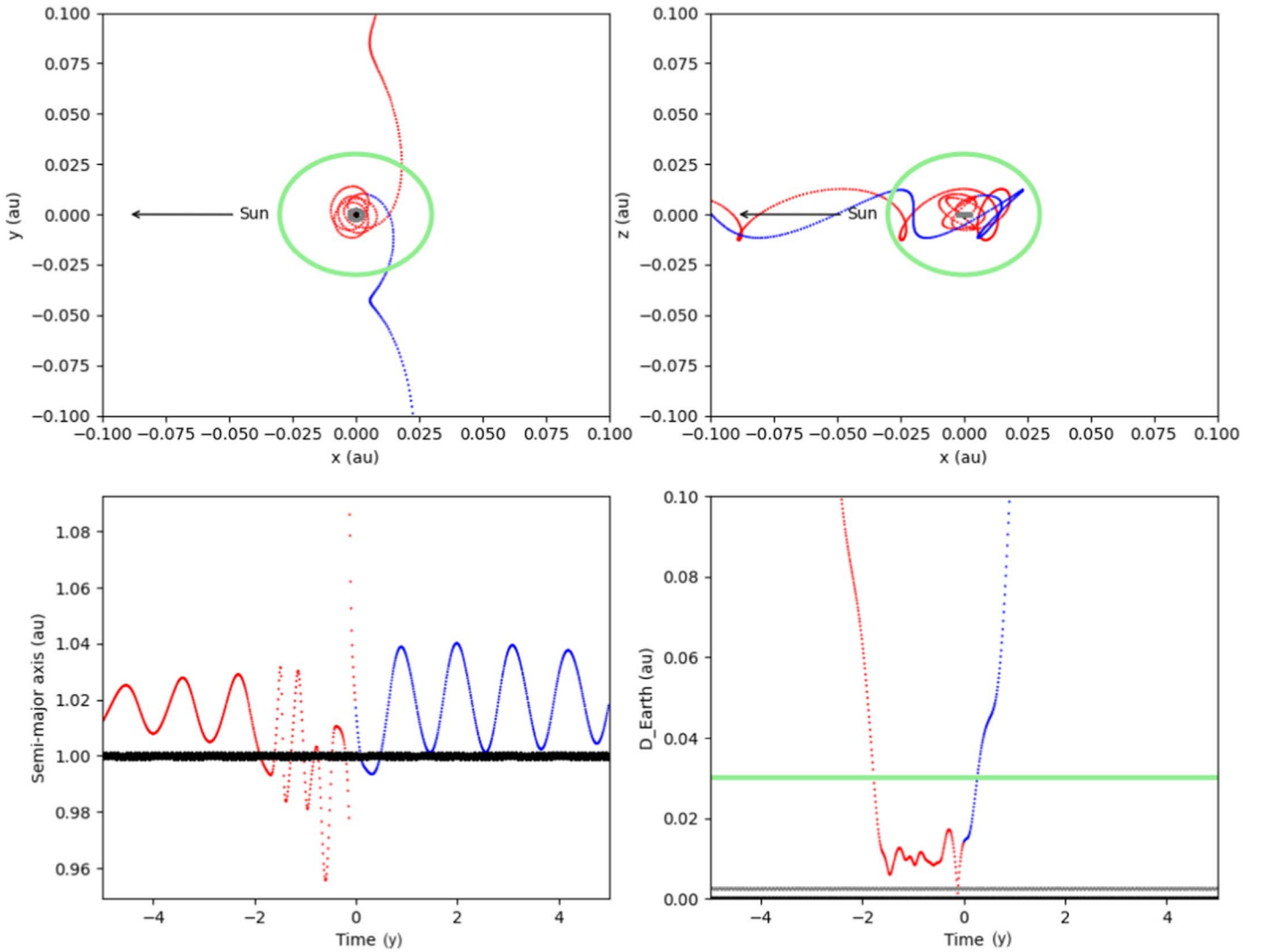
3.4. Orbital Evolution

The second known minimoon, 2020 CD_3, was discovered while it was captured by the Earth–Moon system. To determine its orbital evolution before, during, and after its captured state, we implemented the rebound n-body orbit integration package (Rein & Liu 2012) with our fitted orbit from Table 3. In addition to its nominal orbit, we cloned ~ 10 additional massless test particles defined from the vertices of a cuboid represented by the heliocentric orbital elements and σ orbital parameter semimajor axis a, eccentricity e, and inclination i uncertainties listed in Table 3 and an initial ephemeris time of 2020 March 23 UTC. The simulations are run using the IAS15 integrator (Rein & Spiegel 2015), the Sun, and eight major masses of the solar system, along with the Moon, Vesta, Ceres, and Pluto.[29] The simulations were run using a time step of 0.00249 yr (21.825 hr, 0.03 times the lunar orbital period), with an output of 0.01 yr for 5 and 100 yr time frames.

We adopt the definition of geocentric capture from Fedorets et al. (2017) and Jedicke et al. (2018) to describe the geocentric orbital evolution of 2020 CD_3, namely that, while captured, 2020 CD_3 remains within 3 Hill radii (~ 0.03 au) of the Earth, has an $e_g < 1$, and approaches the Earth to within 1 Hill radius (~ 0.01 au) at some point during its captures. As seen in Figure 6, 2020 CD_3 approaches the Earth–Moon system opposite from the Sun's direction in the direction of the L2 Lagrange point, with its capture beginning in mid-2018 with a low ~ 1 km s^{-1} encounter velocity. Almost half of minimoons pass through the L2 Lagrange point while becoming temporarily geocentrically bound (Granvik et al. 2012); therefore, it seems that 2020 CD_3's capture is nonexceptional in the case of temporarily captured asteroids. In addition, we see from the top panels of Figure 6 that 2020 CD_3 is captured on a retrograde orbit of $\sim 100°$ and completes $\sim$five revolutions around the

---

[29] Taken from the JPL HORIZONS Solar System Dynamics Database, https://ssd.jpl.nasa.gov/ (Giorgini et al. 1996), on 2020 April 10.
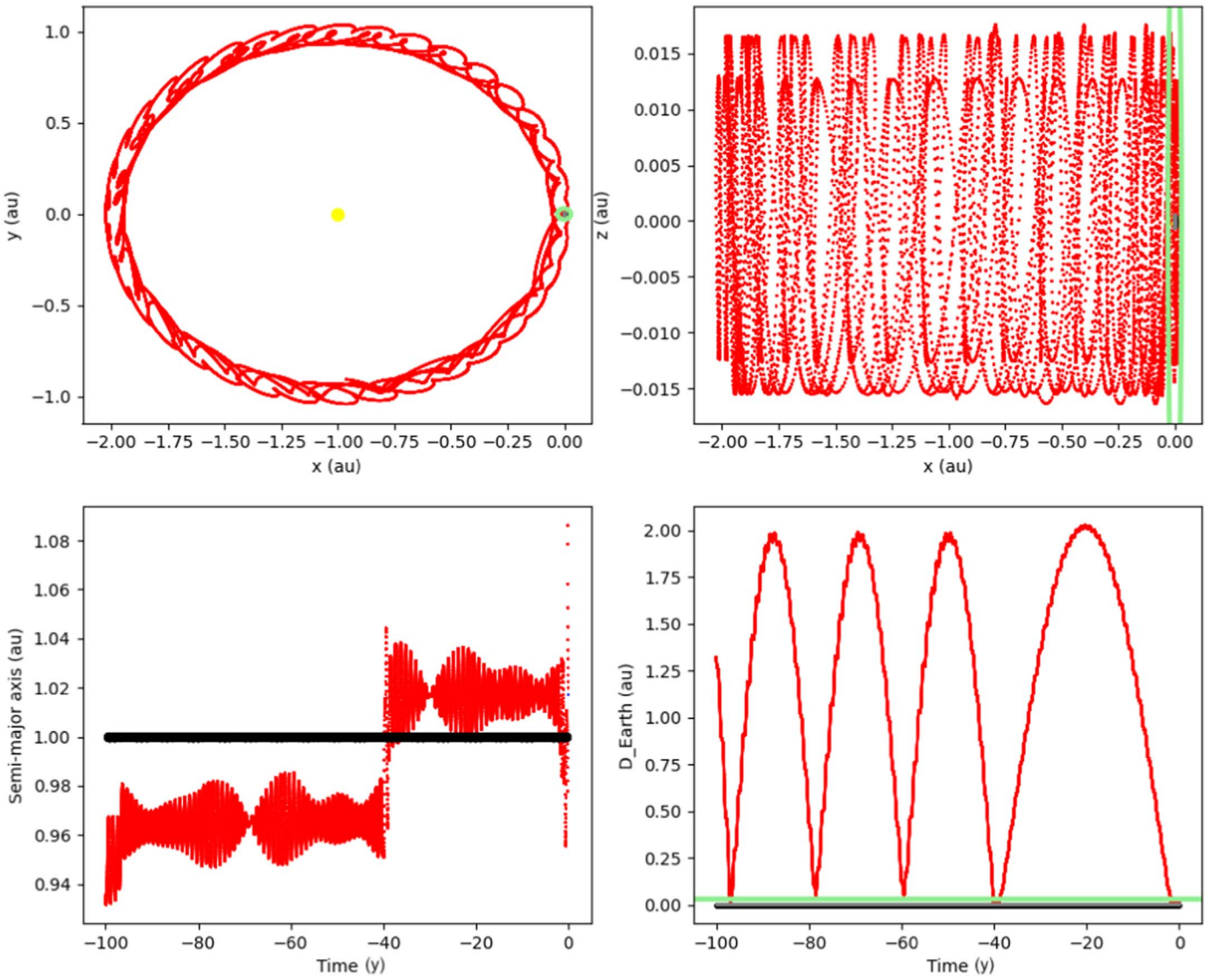
Figure 6. Top left panel: mean geocentric corotating Cartesian y and x coordinates of 2020 CD$_3$ orbital clones ± 5 yr centered on 2020 March 23 UTC encompassing its $\sim$700 day capture completing $\sim$five revolutions around the Earth–Moon system. The red dotted line indicates the trajectory of 2020 CD$_3$ before 2020 March 23 UTC, and the blue dotted line indicates the trajectory of 2020 CD$_3$ after 2020 March 23 UTC. A green circle with a radius of three times the Earth's Hill radii of $\sim$0.03 au is overplotted. The direction toward the Sun in the corotating frame is indicated. Top right panel: same as the top left panel except for mean geocentric corotating Cartesian x and z coordinates. Bottom left panel: evolution of 2020 CD$_3$'s orbital clones' mean semimajor axes ± 5 yr centered on 2020 March 23 UTC. The color code of the dotted lines is the same as in the top panels. Bottom right panel: mean geocentric distance of 2020 CD$_3$ orbital clones ± 5 yr centered on 2020 March 23 UTC. A horizontal green line indicates three times the Hill radii in distance. The color code of the dotted lines is the same as in the previous three panels.

Earth–Moon system while remaining within 3 Hill radii of geocenter. Integrating its orbit forward and backward, the majority of 2020 CD$_3$ orbital clones remained captured within the Earth–Moon system for $\sim$2 yr, as seen in the bottom right panel of Figure 6 leaving the Earth–Moon system in mid-2020. Integrating the orbit with and without a solar radiation pressure component does not significantly affect the capture duration of 2020 CD$_3$. The geocentric orbit of 2020 CD$_3$ is retrograde for nearly the entirety of its capture, and its final orbit will result in it having a slightly larger heliocentric semimajor axis a of 1.027 au compared to its precapture a of 0.973 au, as seen in the bottom left panel of Figure 6. Overall, it seems the capture of 2020 CD$_3$ is typical, having a longer duration than the $\sim$1 yr capture duration of 2006 RH$_{120}$, the only other known minimoon, and an $\sim$9 month capture duration averaged over the minimoon population (Granvik et al. 2012).

In addition, we take a look at the longer-term, 100 yr heliocentric orbital evolution of 2020 CD$_3$ as presented in Figures 7 and 8. Integrating the orbit of 2020 CD$_3$ 100 yr into the past and future shows similar behavior in that 2020 CD$_3$ has close encounters with the Earth, placing it inside the Hill radius of the Earth every $\sim$20–30 yr, as seen in the bottom right panels of Figures 7 and 8. The long-term orbit of 2020 CD$_3$ resembles a horseshoe orbit, as seen in the top left panels of Figures 7 and 8 where its status as temporarily captured asteroids has resulted from its similar orbital plane and low encounter velocity relative to Earth's (Granvik et al. 2013; Jedicke et al. 2018). Interestingly, some of the 2020 CD$_3$ orbit clones, when integrated into the future, switch from a max inclination of 0°.012–0°.031 during the next encounter with the Earth. In addition, we have undertaken preliminary long-term simulations using the hybrid MERCURIUS `rebound` integrator (Rein et al. 2019) using the same initial conditions as above, including the eight clones. These initial simulations indicate that the horseshoe dynamical situation is stable for at least $\sim$10^6 yr.
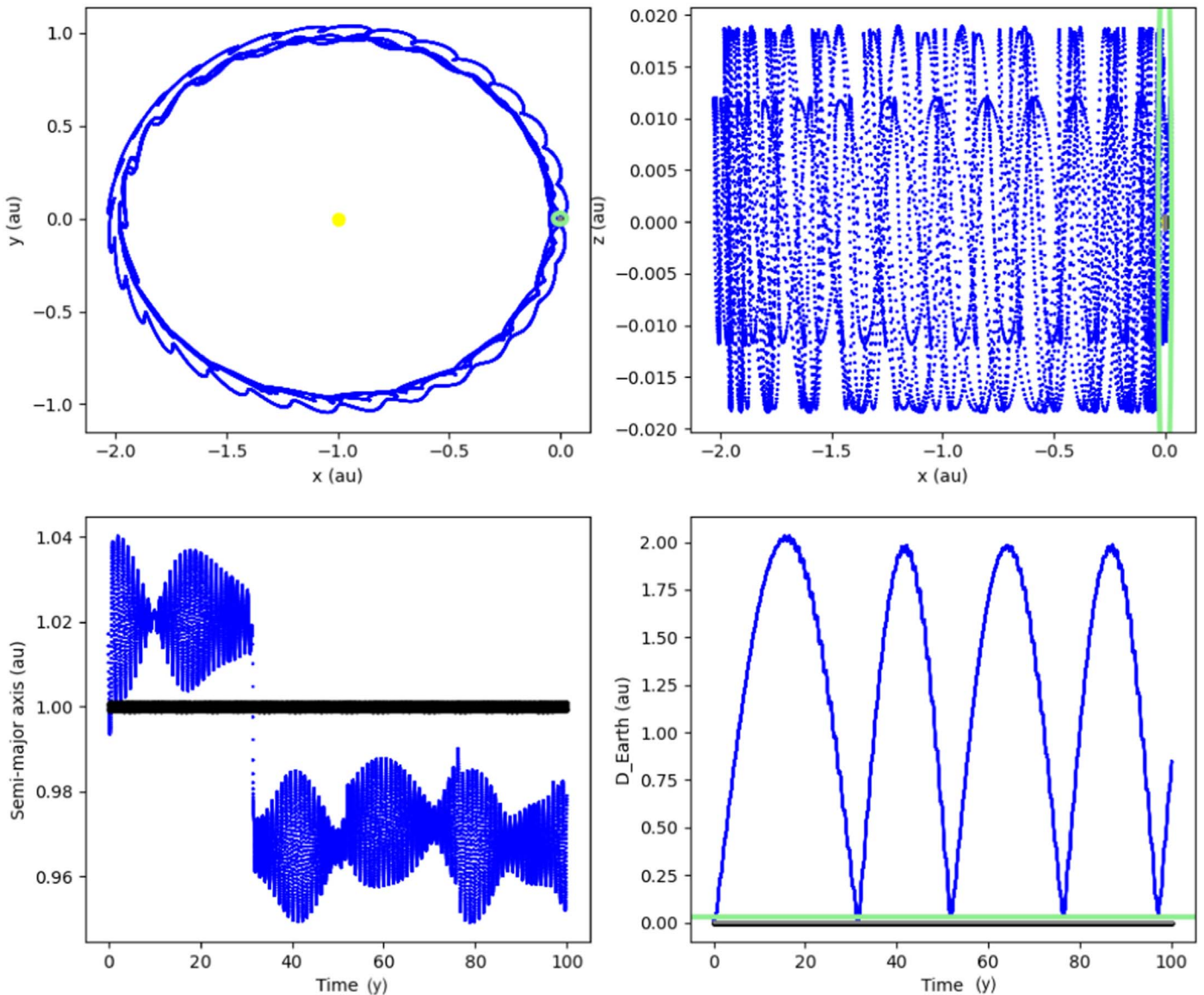
Figure 7. Top left panel: mean geocentric Cartesian y and x coordinates of 2020 CD_3 orbital clones integrated backward 100 yr from 2020 March 23 UTC (red line), with the Earth's three Hill radii marked in green. Top right panel: same as the top left panel except for the mean geocentric Cartesian x and z coordinates of 2020 CD_3 orbital clones integrated backward 100 yr from 2020 March 23 UTC. Bottom left panel: evolution in 2020 CD_3's orbital clones' mean semimajor axis integrated backward 100 yr from 2020 March 23 UTC, with the Earth's orbit in black. Bottom right panel: geocentric distance of 2020 CD_3 orbital clones integrated backward 100 yr from 2020 March 23 UTC.

4. Discussion and Conclusions

It appears that 2020 CD_3 represents a typical case when compared to the known ensemble and dynamical path of minimoons. While it is difficult to estimate the true population of minimoons, given the vast incompleteness of asteroid surveys (Jedicke et al. 2016), the discovery of 2020 CD_3 along with 2006 RH_{120} confirms minimoons as viable members of the NEO population, and CD_3 is the first minimoon to be spectrophotometrically characterized. It seems its orbital dynamics are similar to co-orbitals of Earth (Morais & Morbidelli 2002), of which there is one known example, 2010 TK_7 (Connors et al. 2011), and quasi-satellites, of which several are known, e.g., (469219) 2016 HO_3 (Chodas 2016). Compared to the asteroid population at large, out of ∼1 million known asteroids as of 2020 July, only ∼10 are of similar size as 2020 CD_3 with $H \sim 31$ or smaller, making 2020 CD_3 one of the smallest asteroids discovered and characterized with spectrophotometry (e.g., Reddy et al. 2016).

While its spectrum and colors seem to indicate that 2020 CD_3 is a likely V-type asteroid with an origin in the inner Main Belt (DeMeo & Carry 2013), as discussed in Section 3.1, we can use its orbit in reference to models describing the NEO population (Granvik et al. 2016, 2018) as an independent indication of its source through asteroid escape pathways in the Main Belt (Granvik et al. 2017). Comparison with the NEO population model suggests that its most likely Main Belt escape source with ∼70% probability was through the ν_6 resonance, located near the inner edge of the Main Belt at 2.1 au for low-inclination objects (Milani & Knežević 1990). The second and third most likely sources are the Hungaria asteroid population, located between 1.8 and 2.0 au (Milani et al. 2010) with a ∼25% probability, and the 3:1 mean-motion resonance, located at the border between the inner and center Main Belt at 2.5 au (Wisdom 1983) with a ∼5% probability. We note that the current NEO model is only available for asteroids with H 25 or brighter; therefore, we have made the comparison between

Figure 8. Top left panel: same as Figure 7 except for orbital clones of 2020 CD$_3$ integrated forward 100 yr from 2020 March 23 UTC (blue line), with the Earth's three Hill radii marked in green. Top right panel: same as the top left panel except for the mean geocentric Cartesian x and z coordinates of 2020 CD$_3$ orbital clones integrated forward 100 yr from 2020 March 23 UTC. Bottom left panel: evolution in 2020 CD$_3$'s orbital clones' mean semimajor axis integrated forward 100 yr from 2020 March 23 UTC, with the Earth's orbit in black. Bottom right panel: geocentric distance of 2020 CD$_3$ orbital clones integrated forward 100 yr from 2020 March 23 UTC.

2020 CD$_3$ and the NEO model with the assumption that it has $H = 25$. Its other orbital parameters remain the same for the purposes of comparison with the NEO model.

Weighing the NEO albedo model (Morbidelli et al. 2020) according to these source probabilities for 2020 CD$_3$ results in a predicted albedo, p_v, of $\sim$0.23, which is on the lower end of the 0.25–0.45 p_v range of V-type asteroids (DeMeo & Carry 2013). Using our measured H magnitude of 31.9 ± 0.1 and the following equation relating the diameter D and p_v,

$$D = \frac{1329}{\sqrt{p_v}} 10^{-\frac{H}{5}}, \qquad (5)$$

from Harris & Lagerros (2002), we calculate that 2020 CD$_3$ has $D = 0.9 \pm 0.1$ m using $p_v = 0.35$, the mean albedo of V-type asteroids in the Main Belt (DeMeo & Carry 2013), making it

currently the smallest asteroid studied spectrophotometrically, with the next smallest being asteroid 2015 TC$_{25}$ (Reddy et al. 2016).

We estimate the density of 2020 CD$_3$ by combining our constraints on its diameter and albedo with our AMR measurement from fitting its orbit. Using our measured AMR of $(6.9 \pm 2.4) \times 10^{-4}$ m^2 kg^{-1} and diameter estimate of $D = 0.9 \pm 0.1$ m, we estimate the bulk density of 2020 CD$_3$ to be 2.3 ± 0.8 g cm^{-3}, broadly compatible with the densities of other small asteroids determined from AMR measurements (e.g., Micheli et al. 2012). In comparison, the density of 2015 TC$_{25}$ is $\sim$1 g cm^{-3}, assuming a diameter of $\sim$2.2 m (Reddy et al. 2016) and an AMR of $(6–7) \times 10^{-4}$ m^2 kg^{-1} (Farnocchia et al. 2017). Assuming 0% macroporosity, the total mass of 2020 CD$_3$ is $\sim$10^4 kg.

While its estimated density of 2.3 ± 0.8 g cm^{-3} is broadly consistent with the density of V-type asteroids that have bulk

densities of $\sim$2.3 g cm^{-3} (Carry 2012), which its spectrum resembles, it is likely, however, that 2020 CD$_3$ has a porosity in the range of $\sim$10%–20%, as for meteorites (Consolmagno et al. 2008), its closest analog as one of the smallest known asteroids. In contrast, the kilometer-scale V-type asteroids that we are drawing in comparison with 2020 CD$_3$ have macroporosities of $\sim$30% or larger (Carry 2012), resulting in a higher density when correcting their $\sim$2.3 g cm^{-3} bulk densities for their higher macroporosity. Therefore, it may be more appropriate to compare the density of 2020 CD$_3$ with achondritic basaltic meteorites, which typically have bulk densities of $\sim$3.0 g cm^{-3}, somewhat larger than our estimated range of the density of 2020 CD$_3$.

It is likely that 2020 CD$_3$ is the product of the fragmentation of a larger parent asteroid, given its small $\sim$1 m size and correspondingly short $<$1 Myr timescale (Bottke et al. 2005). There appears to be some discrepancy in the fact that 2020 CD$_3$ most likely originates in the 1.8–2.2 au range at the inner edge of the Main Belt while having a spectrum similar to V-type asteroids, which are thought to originate from the asteroid (4) Vesta (Binzel & Xu 1993; Parker et al. 2008) and are primarily located at $\sim$2.3 au (DeMeo & Carry 2013). A significant number of V-type asteroids exist further from the Sun, located past 2.5 au in the central Main Belt (Carruba et al. 2005; Migliorini et al. 2017), which could provide a possible source of Earth-crossing V-type NEOs like 2020 CD$_3$ if they were to drift inward into the 3:1 resonance due to the thermal recoil Yarkovsky effect (Farinella et al. 1998).

However, the role of the 3:1 resonance in transporting 2020 CD$_3$ into Earth-crossing space from the Main Belt seems unlikely due to its $\sim$5% source probability. In addition, the Yarkovsky effect is able to transport meter-scale objects like 2020 CD$_3$ into the proximity of the ν_6 resonance, the most likely source of 2020 CD$_3$, in $<$1 Myr if it were to have originated as a fragment at 2.3 au (Bottke et al. 2006; Vokrouhlický et al. 2015), where most V-type asteroids are found, even if possesses significantly different thermal inertia properties compared to larger, kilometer-scale asteroids (Delbo et al. 2007; Bolin et al. 2018a). In addition, is apparent from the wide distribution of the $\lesssim$1 km Vesta family fragments covering the entirety of the inner Main Belt (Bolin et al. 2017) that the size-dependent velocity distribution of family fragments originating from Vesta could have placed 2020 CD$_3$–sized objects anywhere between the nu_6 resonance at $\sim$2.2 au and the 3:1 resonance at 3.5 au (Carruba & Nesvorný 2016; Bolin et al. 2018b). Therefore, the location of the ν_6 resonance at the inner edge of the Main Belt at 2.2 au as the most likely source of 2020 CD$_3$ does not necessarily preclude asteroids far from its vicinity as the original parent body of 2020 CD$_3$.

Besides collisions, rotational fission of asteroids that are spinning near their rotational stability limit could be a possible origin of 2020 CD$_3$ (Walsh et al. 2008). Several asteroids have been observed to be in the act of rotationally shedding mass or fragmenting (e.g., Jewitt et al. 2017; Moreno et al. 2017; Ye et al. 2019a) or have a dynamically associated cluster of asteroids compatible with a fragmentation event in the recent past due to their rotation (Vokrouhlický et al. 2017). In addition, binary asteroid systems can become decoupled over time due to the influence of thermal radiation recoil effects (McMahon & Scheeres 2010), which can result in small asteroids like 2020 CD$_3$ leaving their binary systems and entering Earth-crossing space. The fragmentation of asteroid parent bodies or decoupling of binary systems can occur while an asteroid parent body is in NEO space (Scheirich et al. 2019; Bottke et al. 2020), providing an origin for 2020 CD$_3$ outside of the Main Belt.

Another possible origin of minimoons is from lunar impacts. While the orbits of lunar debris dynamically decay after a few kyr, it is possible that some lunar ejecta can be recaptured by the Earth–Moon system as minimoons due to their orbital similarity with the Earth (Gladman et al. 1995). As presented in Figure 3, the spectrum of 2020 CD$_3$ is compatible with the spectrum of bulk lunar rock at the precision of our spectrophotometry. In addition, our inferred density of 2020 CD$_3$ of 2.3 $\pm$ 0.8 g cm^{-3} is similar to impact basin ejecta lunar rock, which has a bulk density ($\sim$2.4 g cm^{-3} Kiefer et al. 2012) and $\sim$20% porosity. Under the assumption that 2020 CD$_3$ originated as lunar ejecta, the young, $\lesssim$1 Myr–scale cosmic-ray exposure ages of lunar meteorites (Eugster et al. 2006) imply that the vast majority of lunar meteorites and, by extension, 2020 CD$_3$ had to have been produced by a large and recent lunar impact. The most recent large impact that could produce ejecta the size of 2020 CD$_3$ is the Giordano Bruno crater, which has been estimated to be $\sim$4 Myr old (Morota et al. 2009) based on the occurrence of craters near its proximity. However, the lunar ejecta origin of 2020 CD$_3$ is diminished by the fact that the vast majority of lunar meteorites possess cosmic-ray exposure ages much shorter than the 4 Myr age of the Giordano Bruno crater, suggesting that the dominant sources of recent lunar meteorites and thus lunar ejecta are much smaller, more recent impact events than could have produced ejecta the size of 2020 CD$_3$ (Minton et al. 2019).

Facilities: Keck I Telescope, P48 Oschin Schmidt telescope/Zwicky Transient Facility.

ORCID iDs

Bryce T. Bolin ⓘ https://orcid.org/0000-0002-4950-6323
Christoffer Fremling ⓘ https://orcid.org/0000-0002-4223-103X
Timothy R. Holt ⓘ https://orcid.org/0000-0003-0437-3296
Matthew J. Hankins ⓘ https://orcid.org/0000-0001-9315-8437
Tomás Ahumada ⓘ https://orcid.org/0000-0002-2184-6430
Varun Bhalerao ⓘ https://orcid.org/0000-0002-6112-7609
Kevin B. Burdge ⓘ https://orcid.org/0000-0002-7226-836X
Chris M. Copperwheat ⓘ https://orcid.org/0000-0001-7983-8698
Michael Coughlin ⓘ https://orcid.org/0000-0002-8262-2924
Kunal P. Deshmukh ⓘ https://orcid.org/0000-0001-5253-3480
Mansi M. Kasliwal ⓘ https://orcid.org/0000-0002-5619-4938
Robert Quimby ⓘ https://orcid.org/0000-0001-9171-5236
Dennis Bodewits ⓘ https://orcid.org/0000-0002-2668-7248
Chan-Kao Chang ⓘ https://orcid.org/0000-0003-1656-4540
Russ R. Laher ⓘ https://orcid.org/0000-0003-2451-5482
Zhong-Yi Lin ⓘ https://orcid.org/0000-0003-3827-8991
Carey M. Lisse ⓘ https://orcid.org/0000-0002-9548-1526
Frank J. Masci ⓘ https://orcid.org/0000-0002-8532-9395
Chow-Choong Ngeow ⓘ https://orcid.org/0000-0001-8771-7554
Chengxing Zhai ⓘ https://orcid.org/0000-0002-0291-4522
Richard Dekany ⓘ https://orcid.org/0000-0002-5884-7867
Dmitry A. Duev ⓘ https://orcid.org/0000-0001-5060-8733
Matthew Graham ⓘ https://orcid.org/0000-0002-3168-0139
Shrinivas R. Kulkarni ⓘ https://orcid.org/0000-0001-5390-8563
Thomas Kupfer ⓘ https://orcid.org/0000-0002-6540-1484
Ashish Mahabal ⓘ https://orcid.org/0000-0003-2242-0244
Reed Riddle ⓘ https://orcid.org/0000-0002-0387-370X
Roger M. Smith ⓘ https://orcid.org/0000-0001-7062-9726
Maayane T. Soumagnac ⓘ https://orcid.org/0000-0001-6753-1488
Lin Yan ⓘ https://orcid.org/0000-0003-1710-9339

References

Barucci, M. A., & Fulchignoni, M. 1982, M&P, 27, 47
Bellm, E. C., Kulkarni, S. R., Graham, M. J., et al. 2019, PASP, 131, 018002
Binzel, R. P., Farinella, P., Zappalà, V., & Cellino, A. 1989, in Asteroids II, ed. R. P. Binzel, T. Gehrels, & M. S. Matthews (Tucson, AZ: Univ. Arizona Press), 416
Binzel, R. P., & Xu, S. 1993, Sci, 260, 186
Bolin, B., Jedicke, R., Granvik, M., et al. 2014, Icar, 241, 280
Bolin, B. T., Delbo, M., Morbidelli, A., & Walsh, K. J. 2017, Icar, 282, 290
Bolin, B. T., & Lisse, C. M. 2020, MNRAS, 497, 4031
Bolin, B. T., Lisse, C. M., Kasliwal, M. M., et al. 2020, AJ, 160, 26
Bolin, B. T., Morbidelli, A., & Walsh, K. J. 2018a, A&A, 611, A82
Bolin, B. T., Walsh, K. J., Morbidelli, A., & Delbo, M. 2018b, MNRAS, 473, 3949
Bolin, B. T., Weaver, H. A., Fernandez, Y. R., et al. 2018c, ApJL, 852, L2
Bottke, W. F., Durda, D. D., Nesvorný, D., et al. 2005, Icar, 179, 63
Bottke, W. F., Moorhead, A., Hergenrother, C. W., et al. 2020, LPI, 51, 1215
Bottke, W. F., Jr., Vokrouhlický, D., Rubincam, D. P., & Nesvorný, D. 2006, AREPS, 34, 157
Bowell, E., Hapke, B., Domingue, D., et al. 1988, in Asteroids II, ed. R. P. Binzel, T. Gehrels, & M. S. Matthews (Tucson, AZ: Univ. Arizona Press), 399
Burdge, K. B., Fuller, J., Phinney, E. S., et al. 2019, ApJL, 886, L12
Bus, S. J., & Binzel, R. P. 2002, Icar, 158, 146
Carruba, V., Michtchenko, T. A., Roig, F., Ferraz-Mello, S., & Nesvorný, D. 2005, A&A, 441, 819
Carruba, V., & Nesvorný, D. 2016, MNRAS, 457, 1332
Carry, B. 2012, P&SS, 73, 98
Chambers, K. C., Magnier, E. A., Metcalfe, N., et al. 2016, arXiv:1612.05560
Chodas, P. 2016, AAS/Division for Planetary Sciences Meeting Abstracts, 48, 311.04
Chyba, M., Patterson, G., Picot, G., et al. 2014, Journal of Industrial and Management Optimization, 10, 477
Connors, M., Wiegert, P., & Veillet, C. 2011, Natur, 475, 481
Consolmagno, G., Britt, D., & Macke, R. 2008, ChEG, 68, 1
Dekany, R., Smith, R. M., Belicki, J., et al. 2016, Proc. SPIE, 9908, 99085M
de la Fuente Marcos, C., & de la Fuente Marcos, R. 2016, MNRAS, 462, 3441
Delbo, M., dell'Oro, A., Harris, A. W., Mottola, S., & Mueller, M. 2007, Icar, 190, 236
DeMeo, F. E., Binzel, R. P., Slivan, S. M., & Bus, S. J. 2009, Icar, 202, 160
DeMeo, F. E., & Carry, B. 2013, Icar, 226, 723
Duev, D. A., Mahabal, A., Ye, Q., et al. 2019, MNRAS, 486, 4158
Durech, J., Carry, B., Delbo, M., Kaasalainen, M., & Viikinkoski, M. 2015, Asteroid Models from Multiple Data Sources (Tucson, AZ: Univ. Arizona Press), 183
Durech, J., Sidorin, V., & Kaasalainen, M. 2010, A&A, 513, A46
Elvis, M., McDowell, J., Hoffman, J. A., & Binzel, R. P. 2011, P&SS, 59, 1408
Eugster, O., Herzog, G. F., Marti, K., & Caffee, M. W. 2006, in Irradiation Records, Cosmic-Ray Exposure Ages, and Transfer Times of Meteorites, ed. D. S. Lauretta & H. Y. McSween (Tucson, AZ: Univ. Arizona Press), 829
Farinella, P., Vokrouhlický, D., & Hartmann, W. K. 1998, Icar, 132, 378
Farnocchia, D., Tholen, D. J., Micheli, M., et al. 2017, AAS/Division for Planetary Sciences Meeting Abstracts, 49, 100.09
Fedorets, G., Granvik, M., & Jedicke, R. 2017, Icar, 285, 83
Fedorets, G., Granvik, M., Jones, R. L., Jurić, M., & Jedicke, R. 2020, Icar, 338, 113517
Flewelling, H. A., Magnier, E. A., Chambers, K. C., et al. 2016, arXiv:1612.05243
Fukugita, M., Ichikawa, T., Gunn, J. E., et al. 1996, AJ, 111, 1748
Gaia Collaboration, Brown, A. G. A., Vallenari, A., et al. 2018, A&A, 616, A1
Gaia Collaboration, Prusti, T., de Bruijne, J. H. J., et al. 2016, A&A, 595, A1
Giorgini, J. D., Yeomans, D., Chamberlin, A., et al. 1996, BAAS, 28, 1158
Gladman, B. J., Burns, J. A., Duncan, M. J., & Levison, H. F. 1995, Icar, 118, 302
Graham, M. J., Kulkarni, S. R., Bellm, E. C., et al. 2019, PASP, 131, 078001
Granvik, M., Jedicke, R., Bolin, B., Chyba, M., & Patterson, G. 2013, in Asteroids: Prospective Energy and Material Resources, ed. V. Badescu (Berlin: Springer), 151
Granvik, M., Morbidelli, A., Jedicke, R., et al. 2016, Natur, 530, 303
Granvik, M., Morbidelli, A., Jedicke, R., et al. 2018, Icar, 312, 181
Granvik, M., Morbidelli, A., Vokrouhlický, D., et al. 2017, A&A, 598, A52
Granvik, M., Vaubaillon, J., & Jedicke, R. 2012, Icar, 218, 262
Gutiérrez, P. J., Davidsson, B. J. R., Ortiz, J. L., Rodrigo, R., & Vidal-Nuñez, M. J. 2006, A&A, 454, 367
Hanuš, J., Delbo, M., Alí-Lagoa, V., et al. 2018, Icar, 299, 84
Hanuš, J., Ďurech, J., Brož, M., et al. 2013, A&A, 551, A67
Harris, A. W., & D'Abramo, G. 2015, Icar, 257, 302
Harris, A. W., Fahnestock, E. G., & Pravec, P. 2009, Icar, 199, 310
Harris, A. W., & Lagerros, J. S. V. 2002, in Asteroids III, ed. W. F. Bottke, Jr (Tucson, AZ: Univ. Arizona Press), 205
Holmberg, J., Flynn, C., & Portinari, L. 2006, MNRAS, 367, 449
Isaacson, P. J., Sarbadhikari, A. B., Pieters, C. M., et al. 2011, M&PS, 46, 228
Ivezić, Ž., Lupton, R. H., Jurić, M., et al. 2002, AJ, 124, 2943
Ivezić, Ž, Tabachnik, S., Rafikov, R., et al. 2001, AJ, 122, 2749
Jedicke, R., Bolin, B., Granvik, M., & Beshore, E. 2016, Icar, 266, 173
Jedicke, R., Bolin, B. T., Bottke, W. F., et al. 2018, FrASS, 5, 13
Jewitt, D., Agarwal, J., Li, J., et al. 2017, AJ, 153, 223

Jordi, K., Grebel, E. K., & Ammon, K. 2006, A&A, 460, 339
Jorgensen, K., Rivkin, A., Binzel, R., et al. 2003, AAS/Division for Planetary Sciences Meeting Abstracts, 35, 36.02
Jurić, M., Ivezić, Ž, Lupton, R. H., et al. 2002, AJ, 124, 1776
Kiefer, W. S., Macke, R. J., Britt, D. T., Irving, A. J., & Consolmagno, G. J. 2012, GeoRL, 39, L07201
Kwiatkowski, T., Kryszczynska, A., Polinska, M., et al. 2008, LPICo, 1405, 8297
Lomb, N. R. 1976, Ap&SS, 39, 447
Masci, F. J., Laher, R. R., Rusholme, B., et al. 2019, PASP, 131, 018003
McMahon, J., & Scheeres, D. 2010, CeMDA, 106, 261
Micheli, M., Tholen, D. J., & Elliott, G. T. 2012, NewA, 17, 446
Micheli, M., Tholen, D. J., & Elliott, G. T. 2013, Icar, 226, 251
Migliorini, A., de Sanctis, M. C., Lazzaro, D., & Ammannito, E. 2017, MNRAS, 464, 1718
Milani, A., & Knežević, Z. 1990, CeMDA, 49, 347
Milani, A., Knežević, Z., Novaković, B., & Cellino, A. 2010, Icar, 207, 769
Minton, D. A., Fassett, C. I., Hirabayashi, M., Howl, B. A., & Richardson, J. E. 2019, Icar, 326, 63
Mommert, M., Hora, J. L., Farnocchia, D., et al. 2014, ApJ, 786, 148
Morais, M. H. M., & Morbidelli, A. 2002, Icar, 160, 1
Morbidelli, A., Delbo, M., Granvik, M., et al. 2020, Icar, 340, 113631
Moreno, F., Pozuelos, F. J., Novaković, B., et al. 2017, ApJL, 837, L3
Morota, T., Haruyama, J., Miyamoto, H., et al. 2009, M&PS, 44, 1115
Moskovitz, N. A., Jedicke, R., Gaidos, E., et al. 2008, Icar, 198, 77
Ofek, E. O. 2012, ApJ, 749, 10
Oke, J. B., Cohen, J. G., Carr, M., et al. 1995, PASP, 107, 375
Parker, A., Ivezić, Ž, Jurić, M., et al. 2008, Icar, 198, 138
Perley, D. A. 2019, PASP, 131, 084503
Press, W. H., Flannery, B. P., & Teukolsky, S. A. 1986, Numerical Recipes. The Art of Scientific Computing (Cambridge: Cambridge Univ. Press)
Pruyne, T. A., Wierzchos, K. W. D. R., Christensen, E., & Farneth, G. 2020, MPEC, 2020-D104, 104

Raab, H. 2012, Astrometrica: Astrometric data reduction of CCD images, Astrophysics Source Code Library, ascl:1203.012
Reddy, V., Sanchez, J. A., Bottke, W. F., et al. 2016, AJ, 152, 162
Rein, H., Hernandez, D. M., Tamayo, D., et al. 2019, MNRAS, 485, 5490
Rein, H., & Liu, S.-F. 2012, A&A, 537, A128
Rein, H., & Spiegel, D. S. 2015, MNRAS, 446, 1424
Rockosi, C., Stover, R., Kibrick, R., et al. 2010, Proc. SPIE, 7735, 77350R
Scheirich, P., Pravec, P., Kušnirák, P., et al. 2019, arXiv:1912.06456
Schunová-Lilly, E., Jedicke, R., Vereš, P., Denneau, L., & Wainscoat, R. J. 2017, Icar, 284, 114
Shao, M., Nemati, B., Zhai, C., et al. 2014, ApJ, 782, 1
Sidorenko, V. V., Neishtadt, A. I., Artemyev, A. V., & Zelenyi, L. M. 2014, CeMDA, 120, 131
Solontoi, M., Ivezić, Ž, Jurić, M., et al. 2012, Icar, 218, 571
Stellingwerf, R. F. 1978, ApJ, 224, 953
Thirouin, A., Moskovitz, N., Binzel, R. P., et al. 2016, AJ, 152, 163
Tingay, S. J., Kaplan, D. L., McKinley, B., et al. 2013, AJ, 146, 103
Tonry, J. L., Stubbs, C. W., Lykke, K. R., et al. 2012, ApJ, 750, 99
Urrutxua, H., & Bombardelli, C. 2017, in International Symp. Space Flight Dynamics 26, ISSFD-2017-074, 1
Vereš, P., & Chesley, S. R. 2017, AJ, 154, 12
Vereš, P., Jedicke, R., Fitzsimmons, A., et al. 2015, Icar, 261, 34
Vokrouhlický, D., Bottke, W. F., Chesley, S. R., Scheeres, D. J., & Statler, T. S. 2015, in Asteroids IV, ed. P. Michel, F. E. DeMeo, & W. F. Bottke (Tucson, AZ: Univ. Arizona Press), 509
Vokrouhlický, D., Pravec, P., Durech, J., et al. 2017, A&A, 598, A91
Walsh, K. J., Richardson, D. C., & Michel, P. 2008, Natur, 454, 188
Warner, B. D., Harris, A. W., & Pravec, P. 2009, Icar, 202, 134
Wisdom, J. 1983, Icar, 56, 51
Ye, Q., Kelley, M. S. P., Bodewits, D., et al. 2019a, ApJL, 874, L16
Ye, Q., Kelley, M. S. P., Bolin, B. T., et al. 2020, AJ, 159, 77
Ye, Q., Masci, F. J., Lin, H. W., et al. 2019b, PASP, 131, 078002
Zappala, V., Cellino, A., Barucci, A. M., Fulchignoni, M., & Lupishko, D. F. 1990, A&A, 231, 548
Zhai, C., Ye, Q., Shao, M., et al. 2020, PASP, 132, 064502